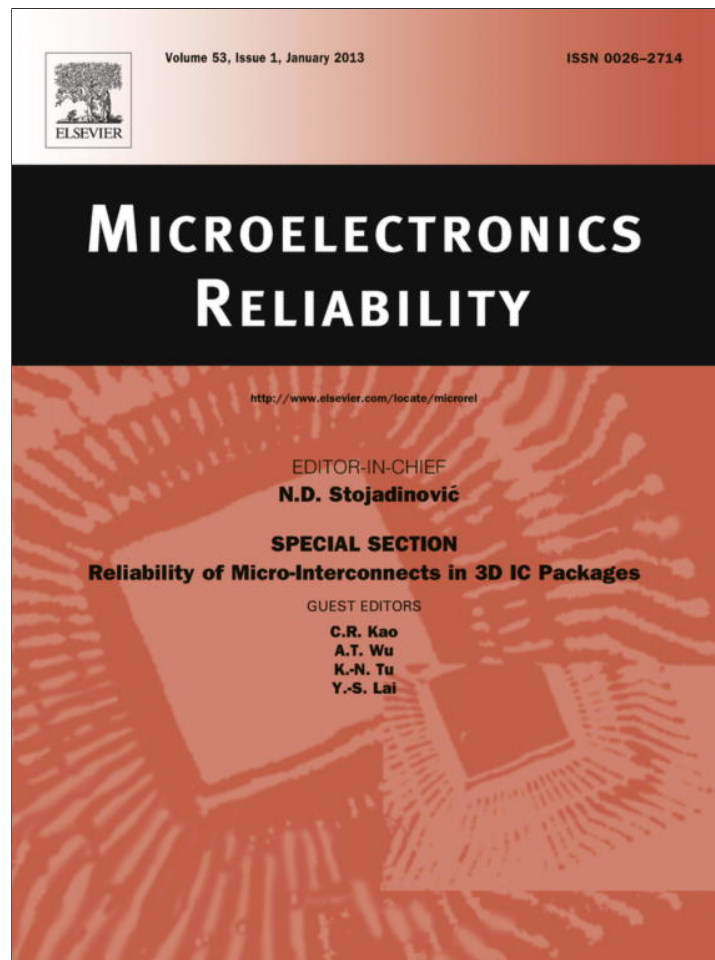


Provided for non-commercial research and education use.
Not for reproduction, distribution or commercial use.



This article appeared in a journal published by Elsevier. The attached copy is furnished to the author for internal non-commercial research and education use, including for instruction at the authors institution and sharing with colleagues.

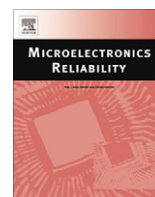
Other uses, including reproduction and distribution, or selling or licensing copies, or posting to personal, institutional or third party websites are prohibited.

In most cases authors are permitted to post their version of the article (e.g. in Word or Tex form) to their personal website or institutional repository. Authors requiring further information regarding Elsevier's archiving and manuscript policies are encouraged to visit:

<http://www.elsevier.com/copyright>

Contents lists available at [SciVerse ScienceDirect](http://www.sciencedirect.com)

Microelectronics Reliability

journal homepage: www.elsevier.com/locate/microrel

Annealing and thickness related performance and degradation of polymer solar cells

Zhouying Zhao, Lynn Rice, Harry Efstathiadis, Pradeep Haldar*

College of Nanoscale Science and Engineering, University at Albany, State University of New York, 255 Fuller Road, Albany, NY 12203, United States

ARTICLE INFO

Article history:

Received 30 May 2011

Received in revised form 29 June 2012

Accepted 2 August 2012

Available online 3 September 2012

ABSTRACT

We investigated annealing and thickness related performance and degradation of bulk heterojunction solar cells based on regioregular poly(3-hexylthiophene) (RR-P3HT):[6,6]-phenyl C61-butyric acid methyl ester (PCBM). The devices were fabricated with slow drying for different active layer thicknesses (100–200 nm thick), followed by an identical thermal annealing. Photoinduced charge carrier generation and dissociation as well as series resistance were extracted from the device current–voltage characteristics and correlated to the active layer absorbance and morphology to understand the behavior of the fabricated devices. It was observed that with slow drying method the thickest absorber device had the highest efficiency but upon the followed thermal annealing it degraded while the thinnest one became substantially improved in performance. For the degraded device the charge carrier generation rate was found nearly unreduced, while the dissociation probability at maximum power voltage and series resistance largely deteriorated with thermal annealing. This implies a likely hampered charge transport and increased recombination losses caused with a discontinuation of the bi-phase networks caused by a further phase separation in the heat treatment. Thus, morphology control for effective charge transport appears crucial to the device performance and stability, and taking into account the active layer thickness effect in annealing is important.

© 2012 Elsevier Ltd. All rights reserved.

1. Introduction

Polymer photovoltaic devices as a potential alternative for low cost conversion of solar energy have attracted intense interest especially since the introduction of bulk-heterojunction (BHJ) of conjugated polymers and fullerene derivatives for efficient charge transfer between the donor and acceptor [1–3]. Power conversion efficiency (PCE) has reached 3–5% with the model system P3HT:PCBM based solar cells [4–6].

An important step for improving the device performance is to enhance microstructure or morphology of the as-spun blend layers, which are typically amorphous due to the co-presence of PCBM with polymer. Thermal annealing [4,5] and latterly demonstrated slow drying or solvent annealing [7,8] have been found to be effective to restore or facilitate the polymer chain organization, which is accompanied with segregation of PCBM, leading to formation of the donor and acceptor rich domains (desirable size at exciton diffusion length, ~10–20 nm) in the blend layer. Upon polymer ordering is a red-shifted absorption and enhanced hole-mobility as a result of π - π stacking interaction of polymer chains and charge carrier delocalization in the formed polymer lamellae [5,7,9]. Correspondingly, the film color changes from orange to purple [10]. This gives rise to an enhanced light absorption of the polymer due to a better spectral matching with the solar emission maxi-

um and a balanced charge transport in the interpenetrating networks.

However, the bi-phase morphology represents a thermodynamically non-equilibrium system [11] and is highly dependent on many factors like the two components ratio of a given material system, solvent used, processing conditions, and especially annealing performed [4,5,12,13]. This presents a challenge in tuning and controlling the morphology with domain sizes at nanoscale of the exciton diffusion length to give rise to a maximally allowable efficiency. For example, if exposed to a high temperature, the device performance may get decreased rather than increased if an excessive domain growth/phase separation takes place [13–16]. Attaining a higher device performance with a better stability through optimization of a single or multiple annealing steps among others is still worth to work on. This requires an in-depth understanding of all these effects, part of which is looked into in the present research to aid in this understanding.

In this work, we present an investigation on the effect of annealing on the performance and degradation of RR-P3HT:PCBM BHJ solar cells as a function of active layer thickness (in the range from 100 nm to 200 nm), with a focus on the device physical behavior. The device active layers were prepared with different spin speeds and slowly dried (with different amounts of residual solvent, depending on the film thickness), and then subjected to an identical thermal annealing. Followed is characterization and comparison of the devices based on their current density–voltage (J - V) characteristics, power conversion efficiency (PCE), ultraviolet

* Corresponding author. Tel.: +1 518 437 8684; fax: +1 518 437 8603.

E-mail address: phaldar@uamail.albany.edu (P. Haldar).

let-visible (UV–vis) absorbance, and atomic force microscopy (AFM) surface topography. Onsager–Braun model based analysis [17,18] was adopted to examine photoinduced charge carrier generation and dissociation in the devices, in combination with series resistance analysis, for understanding the effects of active layer thickness dependent annealing on the absorber morphology and thus device performance and degradation. The results illustrate that the morphology control for attaining effective charge transport is critical to ensure an enhanced device performance and stability, and photocurrent analysis can provide a useful indicator for device and annealing evaluations.

2. Experimental details

The polymer solar cell in this study comprises of an active layer of P3HT:PCBM blend sandwiched between transparent indium tin oxide (ITO) anode and metal cathode. Fig. 1 displays a schematic of P3HT:PCBM organic solar cells along with a picture of the fabricated devices. Before the fabrication process, patterned ITO glass substrates were ultrasonically cleaned in a de-ionized (DI) water bath with detergent, followed by rinsing with DI-water, drying and UV-ozone treatment. A thin layer of poly(3,4-ethylenedioxythiophene) (PEDOT):poly(styrenesulfonate) (PSS) (Baytron P) was spin coated on the ITO surface at 6000 rpm, followed by baking on a hotplate at 170 °C for 4 min in ambient air. The prepared substrates were then transferred into a nitrogen-filled glove box for subsequent processing and current–voltage characterization. A RR-P3HT:PCBM (1:0.6 weight-ratio) solution was made by addition of PCBM (American Dye Source) to a solution of P3HT (Rieke Metals) in 1,2-dichlorobenzene (DCB), 17 mg/ml, and subsequent stirring of the blend at 45 °C for 36 h. P3HT:PCBM active layers were spin coated from the blend solution at speed of 500, 1000 and 1500 rpm for 60 s to form different thicknesses, being wet to nearly dry after the spin process. Each film upon spin coating was placed in a plastic sample container for slow drying (~15 min) at room temperature in the glove box, undergoing a solvent vapor treatment [7,8]. After drying, the films spun at 500, 1000 and 1500 rpm became complete, slight and little purple in colors. Next, a cesium fluoride (~1 nm)/aluminum (40 nm) bi-layers were thermally evaporated on the P3HT:PCBM surface in an

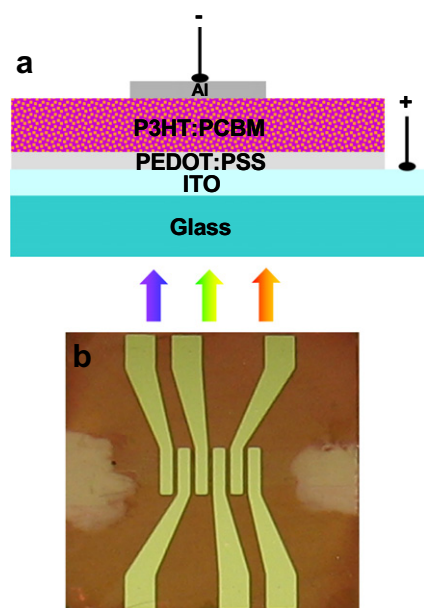


Fig. 1. (a) A schematic of P3HT:PCBM based organic solar cells and (b) a picture of the fabricated devices.

evaporation chamber (base vacuum $<10^{-6}$ Torr) located within the glove box. The completed devices with an active area of 3 mm² were characterized in the glove box with *I*–*V* measurement in both dark and light conditions. The *I*–*V* curves were collected at room temperature with a Keithley 237 source meter, under an illumination condition of AM 1.5G and 100 mW/cm² with using solar light simulator. Then, all devices were thermally annealed on a hotplate at a temperature of 160 °C for 8 min in the glove box, followed by *I*–*V* measurement again in the glove box. Finally, they were transferred to outside of the glove box for additional characterizations in ambient air. Alpha step profilometer was used to determine the P3HT:PCBM active layer thickness of the devices, giving ~200, 160, and 100 nm (with an accuracy of (~5 nm) corresponding to spin speeds of 500, 1000 and 1500 rpm. A Varian Cary 50 UV–vis spectrophotometer was employed to acquire absorbance spectra of the device active layers. A Veeco Digital Imaging Atomic Force Microscope was utilized to take AFM scanning on the device active layer surfaces.

3. Results and discussion

Fig. 2a compares current density–voltage (*J*–*V*) characteristics (AM1.5 illumination) of the slowly dried or solvent annealed P3HT:PCBM BHJ solar cells of 100, 160, and 200 nm active layer thicknesses, named as devices #1–3. The 200 nm absorber device #3 demonstrates the best performance with power conversion efficiency of 3.76% over 2.86% and 3.04% for devices #1–2, owing to its highest short circuit current density (Table 1, in the columns of solvent annealing). Considering that the thin to thick active layers were spun at 1500, 1000, and 500 rpm speeds, there were poor

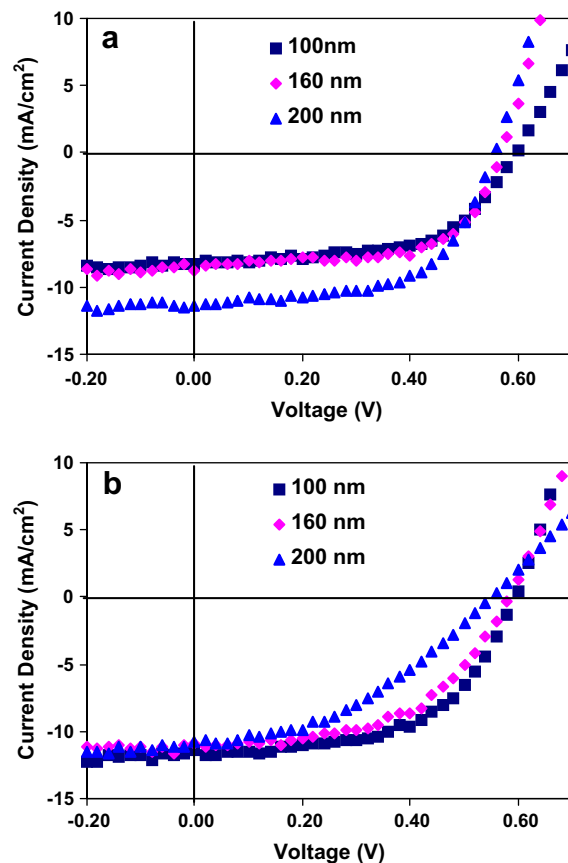


Fig. 2. Current density versus voltage characteristics under AM 1.5G illumination for RR-P3HT:PCBM solar cell devices #1–3 with different active layer thicknesses as marked: (a) solvent treatment and (b) followed thermal annealing.

Table 1

Current density–voltage characteristic parameters of RR:P3HT:PCBM solar cell devices #1–3 with active layer thicknesses of 100 nm, 160 nm, and 200 nm, respectively.

	Device #1		Device #2		Device #3	
	Solvent annealing	Followed thermal annealing	Solvent annealing	Followed thermal annealing	Solvent annealing	Followed thermal annealing
J_{sc} (mA/cm ²)	8.32	11.43	8.82	10.94	11.34	10.81
V_{oc} (V)	0.6	0.6	0.56	0.58	0.56	0.54
FF (%)	57.4	56	61.6	55.1	59.1	40.1
Efficiency (%)	2.86	3.84	3.04	3.49	3.76	2.43

to rich amounts of residual solvent left over for the morphology relaxations. These gave rise to low to high degrees of polymer ordering in the thin to thick dried layers as indicated by their orange, mixed orange/purple, and complete purple colors, respectively. The color is a direct outcome of the polymer microstructure and resultant optical absorption property while film thickness affects just the color intensity for a given microstructure [9,10]. Actually, upon spin coating, all samples had orange color but the thickest film was fully wet and able to undergo sufficient solvent assisted polymer organization turning to purple color when dried while the thinnest film was nearly dried upon the processing with the color basically remained orange, indicative of an amorphous structure. After followed thermal annealing the thickest crystalline film stayed on the purple color despite a morphology evolution, while the other samples changed to complete purple color, in agreement with the final identical absorbance maxima observed from them, which is demonstrated latter. With polymer ordering are improved light absorption, hole mobility, balanced charge transport, and thus enhanced device performances [7,8]. Therefore, the displayed performance trend originates from the thickness dependent morphology effects, consistent with the observation of Chou et al. on inverted polymer/ZnO nanorod hybrid solar cells [19].

To improve the device performances, an identical thermal annealing was carried out at 160 °C for 8 min, which was previously determined to be optimal for single thermal-annealing step treated polymer solar cells fabricated in this lab. It turned out that the best photovoltaic performance was then obtained with the 100 nm absorber device upon thermal annealing (Fig. 2b). Table 1 (in the columns of followed thermal annealing) exhibits details that after thermal annealing device #1 has a profoundly improved efficiency of 3.84% due to a large increase in J_{sc} while device #3 has an unexpected efficiency drop to 2.43% with a large drop in fill factor FF , and device #2 has a slightly increased efficiency of 3.49% owing to the increases in J_{sc} and open circuit voltage V_{oc} and a competing decrease in FF . These outcomes are not fully expected instead display combined effects of active layer thickness associated solvent treatment and thermal annealing on the device performance as compared to thermal annealing induced improvement or aging of polymer solar cells [4,14].

The trends were repeated for other 5–6 sets of devices of the same active layer thickness serial (constructed on one substrate at the same time) as shown in Fig. 3. The average efficiencies derived from these 100, 160 and 200 nm absorber devices are, respectively, $2.1 \pm 0.69\%$, $3.1 \pm 0.13\%$, and $3.7 \pm 0.09\%$ before thermal annealing or with solvent vapor treatment, in contrast to $3.8 \pm 0.21\%$, $3.5 \pm 0.38\%$, and $2.6 \pm 0.43\%$ after thermal annealing.

To explain the above device behaviors, photocurrent analysis was employed to get the optoelectronic physics of the devices before and after thermal annealing [20,21]. Fig. 4 exhibits photocurrent density J_{ph} , obtained from subtraction of the current density in dark (not shown) from that in light (Fig. 2), as a function of effective voltage $V_{eff} = V_o - V$, where V_o (e.g. 0.6 V) is the compensation voltage at which light current equals dark current and V is applied bias. It is noticeable that in the log–log plot J_{ph} increases linearly

with voltage in the low effective field region (e.g. $V_{eff} < 0.2$ V) and turns to gradually saturate with voltage in the high effective field region ($V_{eff} \geq 0.2$ V). At $V_{eff} \sim 1.6$ V (or $V = -1$ V), J_{ph} , for each device is closer to saturations, which means that majority of photoinduced electron–hole pairs dissociate into free charge carriers from bound geminate pairs of holes on the donor and electrons on the acceptor. Thus, in this second region, according to Onsager–Braun model of ion–pair dissociation in weak electrolytes [17,18], electric-field and temperature dependent free charge generation rate $G(E,T)$ and dissociation probability $P(E,T)$ can be estimated from $J_{ph}(E,T) = qG(E,T)L = qG_{max}P(E,T)L$, with q the electric charge, L the absorber thickness, and G_{max} the maximal generation rate of free charges at a large reverse bias [20].

In this work, we adopted this method but differently calculated $P(E,T)$ from $J_{ph}(E,T) = qG_{-1}P(E,T)L$, where $J_{ph}(E,T)$ is given in Fig. 4 in the region of $V_{eff} \geq 0.2$ V and G_{-1} is calculated from $J_{ph}(-E,T) = qG(E,T)L$ at $V_{eff} \sim 1.6$ V or applied voltage $V \sim -1$ V, and thus the obtained dissociation probability is a relative value to that at -1 V. Listed in Table 2 are generation rate G_{-1} at bias of -1 V and relative dissociation probabilities P_0 at short circuit voltage ($V = 0$ V) and P_{mp} at maximum power voltage (e.g. $V = \sim 0.4$ V). Also included in the table is series resistance R_s , determined with the method given in [22] from dark J - V characteristics of the solar cells. Specifically, the series resistance (R_s) is derived from log dark current density versus log voltage curve with using $R_s = \Delta V/J$, where ΔV is the voltage offset from the linearity at high bias and J is the current density. As shown, for each device either before or after thermal annealing, the dissociation probability decreases with diminishing of effective voltage or built-in field in the active layer. For example, for device #3 with solvent annealing, relative to that at -1 V, the dissociation probabilities are 88.9% and 70.8% at short circuit and maximum power voltages, respectively. P_{mp} is directly proportional to power conversion efficiency and the decrease in dissociation probability reflects losses of photogenerated charge carriers. It is argued that the charge loss in the transport and dissociation process could be caused by the recombination of weakly bound geminate pairs or free electrons and holes (bimolecular pairs) or both [20,23,24].

Fig. 4 shows that with slow drying the 200 nm thick absorber device #3 has the highest photocurrent density in the quasi saturation region as compared to that of devices #1–2, due to the better optical absorption and hole-mobility in the thicker layer resulting from its higher degree of solvent annealing and polymer ordering. Importantly, this device also processes relatively high P_0 and P_{mp} and low series resistance (Table 2, solvent annealing) despite its largest thickness, indicating lower charge carrier recombination losses at short circuit and maximum power voltages. This is likely attributed to the polymer ordering and suitable phase separation (domain size ideally at 10–20 nm) with still continuous bi-phase networks, allowing efficient charge separation and transports [21,26]. Accordingly, the observed performance differences between the slowly dried devices are the results of their thickness dependent solvent treatments on their morphologies or polymer ordering and interpenetrating networks. While a vertical phase separation with P3HT and PCBM enrichments at cathode and an-

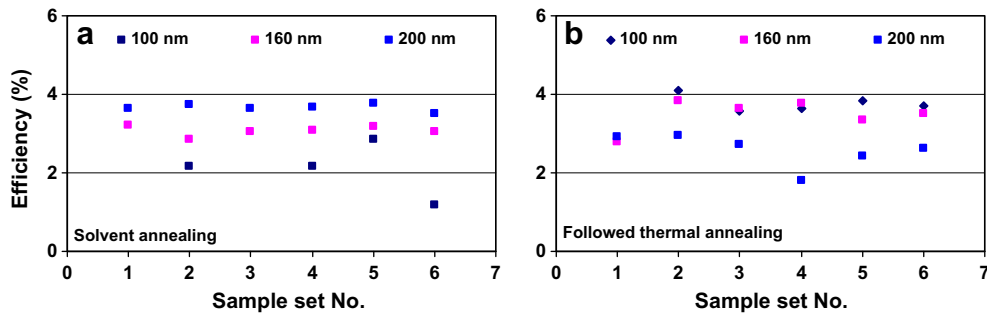


Fig. 3. Power conversion efficiency of six sets of RR-P3HT:PCBM solar cells with different active layer thicknesses as marked: (a) solvent treatment and (b) followed thermal annealing.

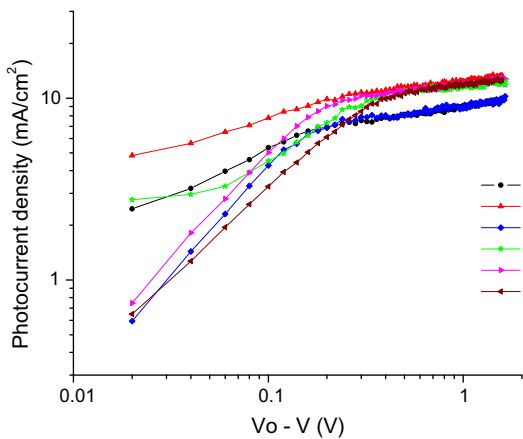


Fig. 4. Photocurrent density as a function of effective bias for the RR-P3HT:PCBM solar cells, where labels (B, D), (F, H), and (J, L) are for devices #1–3 with solvent annealing and followed thermal annealing, respectively.

ode, respectively, is typical of this material system [25], it should generate no difference between all the layers as this is dependent on the surface energy difference of the absorber components and their interactions with substrates, which are the same for the layers prepared.

Followed thermal annealing greatly improved the behavior of the thinnest 100 nm absorber device #1 as seen from the improved photocurrent density at the similarly high level to that of device #3 in the quasi saturation region (Fig. 4) or from the increased G_{-1} of $8.09 \times 10^{27} \text{ m}^{-3} \text{ s}^{-1}$ (Table 2). This is contributed by the large enhancement in polymer chain alignment from the less ordered or amorphous structure of the layer before thermal annealing. The polymer crystallization is evident from the layer color change from orange to purple or more clearly from the UV–vis absorbance spectra (Fig. 5) collected after thermal annealing, which display overwhelming red-shifted peaks (at 508 nm) with distinguishable vibronic shoulders (at ~ 550 and 600 nm) as compared to that of amorphous structure [9], due to interchain π overlap with polymer ordering. The identical peak positions for all devices are indicative

of the same level of polymer organization in them while the variation of the peak intensity is a function of film thickness. This is also confirmed by the AFM images of the thermally annealed layers (Fig. 6), which display their similar fibrillar features typical of polymer crystalline domains [26]. In addition, a possible PCBM segregation at the aluminum interface with thermal annealing may be one more contributing effect for an enhanced electron collection according to the reported investigations [27,28]. Table 2 further reveals that P_0 and P_{mp} of device #1 greatly increase (up to 76.2% in P_{mp} , for example) while R_s correspondently decreases, suggesting improved hole-mobility for efficient charge transport and resultant low losses [7,8]. This affords a further meaningful reason for the profound improvement of efficiency with this device after thermal annealing. Note that although the R_s decreased, the fill factor of this device slightly decreased from 57.4% to 56% (Table 1) rather than increased due to a decreased shunting (see Fig. 2) for this thinner layer device after thermal annealing [29]. In comparison, device #2 experienced lower enhancements in G_{-1} and P_0 with thermal annealing since the medium thick absorber initially underwent more residual solvent treatment and polymer ordering than device #1.

In contrast, device #3 with the followed thermal annealing came up with a large drop in P_{mp} (to 61.3%) and a slight drop in P_0 (Table 2) but with little reduction in G_{-1} (or saturating J_{ph}). Morphologically, after thermal annealing the absorber of this device is seen much rougher than that of devices #1–2 as exhibited by the AFM topography images shown in Fig. 6. This suggests large domains/phase separation with device #3 after thermal annealing while its earlier morphology may be at a suitable shape according to the device decent fill factor before thermal annealing. Previous studies have shown that AFM morphology of P3HT:PCBM blend films is smoother at as-prepared state but becomes rougher with annealing treatment [30,31]. A domain growth is expected to continuously take place in annealing as a result of the high tendency of P3HT and PCBM to de-mix in the non-equilibrium blend system, with a resultant rough morphology formation [7,11,14]. However, the observed performance degradation with thermal annealing for the device studied is not mainly attributed to domain growth induced less interfacial area for charge transfers as compared to that

Table 2
Photoinduced charge carrier generation rate G_{-1} at bias of -1 V and dissociation probabilities P_0 at short circuit voltage ($V = 0$ V) and P_{mp} at maximum power voltage (e.g. $V = \sim 0.4$ V), referenced to that at -1 V, and series resistance R_s for RR-P3HT:PCBM solar cell devices #1–3 with active layer thicknesses of 100 nm, 160 nm, and 200 nm, respectively.

	Device #1		Device #2		Device #3	
	Solvent annealing	Followed thermal annealing	Solvent annealing	Followed thermal annealing	Solvent annealing	Followed thermal annealing
$G_{-1} (\text{m}^{-3} \text{ s}^{-1})$	6.10×10^{27}	8.09×10^{27}	3.97×10^{27}	4.89×10^{27}	3.99×10^{27}	3.90×10^{27}
$P_0 (\%)$	85.3	88.4	86.8	87.3	88.9	86.7
$P_{mp} (\%)$	67.5	76.2	75.5	69.1	70.8	61.3
$R_s (\Omega \text{ cm}^2)$	18.8	4.3	4.2	6.8	5.3	100

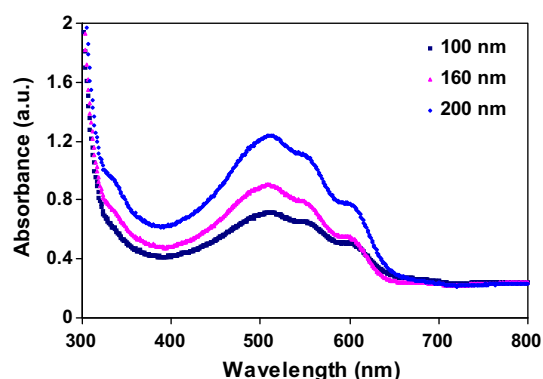


Fig. 5. UV-vis absorbance spectra of the solvent and thermally annealed RR-P3HT:PCBM active layers of 100, 160 and 200 nm thicknesses for devices #1–3.

in [14], where the authors reported an apparent reduction in short circuit current. Likewise, the degradation is less associated with a possible deterioration of the electrical contact between the organic layer and aluminum electrode with surface roughening and chemical effects as discussed in [15,16], in view of the fact that the G_{-1} presented here remains nearly unchanged after thermal annealing. Instead, the drop in the dissociation probabilities and thus efficiency is most likely attributed to a discontinuation of charge percolations caused by a further domain growth/phase separation in the followed thermal annealing and consequent more recombination losses [21,26], in agreement with the study carried out with scanning-probe microscopy by Huang et al. [32]. Furthermore, the thermal annealing induced large drop in the dissociation probability at merely maximum power voltage or $V_{eff,mp}$ (a lower internal field) for P_{mp} not at short circuit voltage or $V_{eff,0}$ (a higher internal field) for P_0 in the device implies probably bimolecular recombination dominated losses, as this is weak at $V_{eff,0}$ but becomes stronger toward $V_{eff,mp}$ according to device modeling [26,33]. Supportive of this is the strikingly increased R_s of device #3 (from 5.3 to 100 $\Omega \text{ cm}^2$ after thermal annealing), which advises a retarded charge hopping between domains and thus an increased bi-molecular recombination as in this case there are only injected bi-molecular charge carriers involved. It is also confirmed by the space charge limited transport (see the substantial drop in fill factor to 40.1% listed in Table 1) due to charge built-up in the hampered transport networks [34].

Similar effects occurred to device #2 as reflected from the deteriorations in P_{mp} and R_s and correspondently in FF (Tables 1 and 2), despite the overall slight improvement in efficiency owing to the enhanced polymer ordering with thermal annealing. However, the impairment in the charge transport of device #2 is hard to perceive from the AFM morphology that is nearly the same smooth as that of device #1 (Fig. 5). This may illustrate that polymer solar cell performance strongly relies on the blend morphologies in terms of nanoscale size and shape of phase-separated regions and thus percolations of charges [35]. This is stringent for the devices with thicker absorbers because charge carrier recombination increases with the thickness or distance that the charges need to traverse to their respective electrodes. For instance, the overall net generation rates of device #3 (Table 2) are lower due to its larger absorber thickness related lower internal electrical field and higher series resistance (after thermal annealing).

According to the reported carrier mobility (say 0.0056 cm^2/Vs for holes before anneal) and lifetime of milliseconds timescale [28,36], the carrier drift or diffusion length under the effective voltages (e.g. 0.6 V) is larger than the phase separated domain size and the studied active layer thickness (100–200 nm) and should pro-

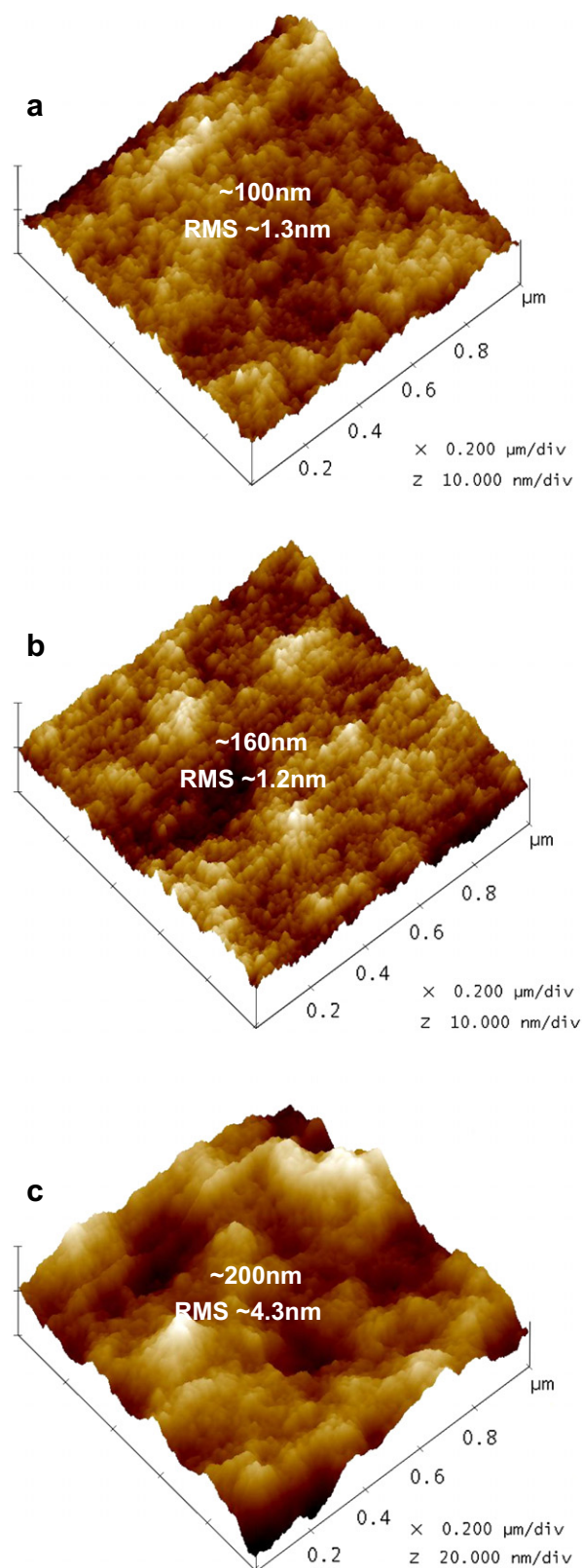


Fig. 6. AFM topography images of the solvent and thermally annealed RR-P3HT:PCBM active layers of thicknesses: (a) 100 nm, (b) 160 nm, and (c) 200 nm for devices #1–3, with root mean square (RMS) surface roughness as marked.

duce no differences between the device performances. The fact is that the charge carrier transport comprises of diffusion within the domains and hopping between domains [7,21,26], the latter

of which largely affects the device performance. The network formation and evolution and the associated charge transport is dependent on both the thickness related solvent annealing and thermal annealing and affects the observed performance trends and thus is within the focus of the discussion presented here.

The above results and analysis illustrate the importance for optimization and stabilization of the ultimate morphology involving the combined effects of the layer thickness and annealing on polymer ordering, interpenetrating networks, charge transport, and recombination. It is noteworthy that the dissociation probability at maximum power voltage, P_{mp} , and series resistance, R_s , are found simultaneously changing and closely correlated to the device efficiency. These two parameters appear as a practicable indicator of the intermixing degree of the donor and acceptor and the status of the affiliated charge transport and recombination in bulk heterojunction solar cells. Though crystallizations enable enhanced charge carrier mobility within domains, excessive domain growth/phase separation tends to significantly influence charge hopping capability and interfacial charge transfer between domains, which are some essential factors of the device degradation or instability and can be analyzed with extractions of the photocurrent related parameters in conjunction with series resistance for potential control or mitigation of the active layer morphology.

4. Conclusion

It has been demonstrated that RR-P3HT:PCBM bulk heterojunction solar cells have different performance characteristics to annealing depending on the absorber thickness. The studied devices with a slow drying method show increased efficiencies with active layer thickness due to increased residual solvent annealing giving rise to a better crystallization and phase separation kinetics in the thicker absorber. With followed thermal annealing the thinner absorber device was improved in morphology and thus in performance while the thicker one became degraded as the high tendency of P3HT crystallization caused PCBM molecules to further segregate, reducing the continuation of the charge percolation networks and charge transport efficiency with consequent more recombination losses of charges. Thus, morphology control combining annealing and active layer thickness effects is worthwhile for improving the device performance and possibly stability.

Acknowledgements

The authors would like to thank Dr. George G. Malliaras and his research group at Cornell University for support of the partial experiments. Funding for this project was provided by a grant from the National Aeronautics and Space Administration.

References

- [1] Sariciftci NS, Smilowitz L, Heeger AJ, Wudl F. Photoinduced electron transfer from a conducting polymer to buckminsterfullerene. *Science* 1992;258:1474–6.
- [2] Yu G, Gao J, Hummelen JC, Wudl F, Heeger AJ. Polymer photovoltaic cells: enhanced efficiencies via a network of internal donor–acceptor heterojunctions. *Science* 1995;270:1789–91.
- [3] Brabec CJ, Sariciftci NS, Hummelen JC. Plastic solar cells. *Adv Funct Mater* 2001;11:15–26.
- [4] Al-Ibrahim M, Ambacher O, Sensfuss S, Gobsch G. Effects of solvent and annealing on the improved performance of solar cells based on poly(3-hexylthiophene):fullerene. *Appl Phys Lett* 2005;86:201120/1–3.
- [5] Ma W, Yang C, Gong X, Lee K, Heeger AJ. Thermally stable, efficient polymer solar cells with nanoscale control of the interpenetrating network morphology. *Adv Funct Mater* 2005;15:1617–22.
- [6] Xiao T, Cui W, Anderregg J, Shinar J, Shinar R. Simple routes for improving polythiophene:fullerene-based organic solar cells. *Org Electron* 2011;12:257–62.
- [7] Li G, Shrotriya V, Huang J, Yao Y, Moriarty T, Emery K, et al. High-efficiency solution processable polymer photovoltaic cells by self-organization of polymer blends. *Nat Mater* 2005;4:864–8.
- [8] Zhao Y, Xie Z, Qu Y, Geng Y, Wang L. Solvent-vapor treatment induced performance enhancement of poly(3-hexylthiophene):methanofullerene bulk-heterojunction photovoltaic cells. *Appl Phys Lett* 2007;90:043504/1–3.
- [9] Brown PJ, Thomas DS, Kohler A, Wilson JS, Kim J-S, Ramsdale CM, et al. Effect of interchain interactions on the absorption and emission of poly 3-hexylthiophene. *Phys Rev B* 2003;67:64203/1–16.
- [10] Qin D, Quan W, Cheng C, Liu J, Zhang J. The optimized morphology of polymer:fullerene bulk heterojunction thin film via reducing pressure. *Semicond Sci Technol* 2010;25:095003/1–4.
- [11] Miyanishi S, Tajima K, Hashimoto K. Morphological stabilization of polymer photovoltaic cells by using cross-linkable poly(3-(5-hexenyl)thiophene). *Macromolecules* 2009;42:1610–8.
- [12] Bettignies RD, Leroy J, Firon M, Sentein C. Accelerated lifetime measurements of P3HT:PCBM solar cells. *Synth Met* 2006;156:510–3.
- [13] Bertho S, Haelderms I, Swinnen A, Moons W, Martens T, Lutsen L, et al. Influence of thermal ageing on the stability of polymer bulk heterojunction solar cells. *Sol Energy Mater Sol Cells* 2007;91:385–9.
- [14] Bertho S, Janssen G, Cleij TJ, Conings B, Moons W, Gadisa A, et al. Effect of temperature on the morphological and photovoltaic stability of bulk heterojunction polymer:fullerene solar cells. *Sol Energy Mater Sol Cells* 2008;92:753–60.
- [15] Reese MO, Morfa AJ, White MS, Kopidakis N, Shaheen SE, Rumbles G, et al. Pathways for the degradation of organic photovoltaic P3HT:PCBM based devices. *Sol Energy Mater Sol Cells* 2008;92:746–52.
- [16] Paci B, Generosi A, Bailo D, Albertini VR, de Bettignies R. Discriminating bulk, surface and interface aging effects in polymer-based active materials for efficient photovoltaic devices. *Chem Phys Lett* 2010;494:69–74.
- [17] Onsager L. Deviations from Ohm's law in weak electrolytes. *J Chem Phys* 1934;2:599–615.
- [18] Braun CL. Electric field assisted dissociation of charge transfer states as a mechanism of photocarrier production. *J Chem Phys* 1984;80:4157–61.
- [19] Chou C-Y, Huang J-S, Wu C-H, Lee C-Y, Lin C-F. Lengthening the polymer solidification time to improve the performance of polymer/ZnO nanorod hybrid solar cells. *Sol Energy Mater Sol Cells* 2009;93:1608–12.
- [20] Mihailetchi VD, Koster LJA, Hummelen JC, Blom PWM. Photocurrent generation in polymer–fullerene bulk heterojunctions. *Phys Rev Lett* 2004;93:216601/1–4.
- [21] Mihailetchi VD, Wildeman J, Blom PWM. Space-charge limited photocurrent. *Phys Rev Lett* 2005;94:126602/1–4.
- [22] Johnston Jr WD. *Solar voltaic cells*. New York: Marcel Dekker Inc; 1980.
- [23] Montanari I, Nogueira AF, Nelson J, Durrant JR, Winder C, Loi MA, et al. Transient optical studies of charge recombination dynamics in a polymer/fullerene composite at room temperature. *Appl Phys Lett* 2002;81:3001–3.
- [24] Shuttle CG, O'Regan B, Ballantyne AM, Nelson J, Bradley DDC, Durrant JR. Bimolecular recombination losses in polythiophene:fullerene solar cells. *Phys Rev B* 2008;78:113201/1–4.
- [25] Xu Z, Chen L-M, Yang G, Huang C-H, Hou J, Wu Y, et al. Vertical phase separation in poly(3-hexylthiophene):fullerene derivative blends and its advantage for inverted structure solar cells. *Adv Funct Mater* 2009;19:1227–34.
- [26] Savenije TJ, Kroeze JE, Yang X, Loos J. The formation of crystalline P3HT fibrils upon annealing of a PCBM:P3HT bulk heterojunction. *Thin Solid Films* 2006;511–512:2–6.
- [27] Orimo A, Masuda K, Honda S, Bente H, Ito S, Ohkita H, et al. Surface segregation at the aluminum interface of poly(3-hexylthiophene)/fullerene solar cells. *Appl Phys Lett* 2010;96:043305/1–4.
- [28] Balderrama VS, Estrada M, Cerdeira A, Soto-Cruz BS, Marsal LF, Pallares J, et al. Influence of P3HT:PCBM blend preparation on the active layer morphology and cell degradation. *Microelectron Reliab* 2011;51:597–601.
- [29] Lee M-K, Wang J-C, Horng S-F, Meng H-F. Extraction of solar cell series resistance without presumed current–voltage functional form. *Sol Energy Mater Sol Cells* 2010;94:578–82.
- [30] Pivrikas A, Stadler P, Neugebauer H, Sariciftci NS. Substituting the postproduction treatment for bulk-heterojunction solar cells using chemical additives. *Org Electron* 2008;9:775–82.
- [31] Miller S, Fanchini G, Lin Y-Y, Li C, Chen C-W, Sub W-F, et al. Investigation of nanoscale morphological changes in organic photovoltaics during solvent vapor annealing. *J Mater Chem* 2008;18:306–12.
- [32] Huang Y-C, Liao Y-C, Li S-S, Wu M-C, Chen C-W, Su W-F. Study of the effect of annealing process on the performance of P3HT/PCBM photovoltaic devices using scanning-probe microscopy. *Sol Energy Mater Sol Cells* 2009;93:888–92.
- [33] Koster LJA, Smits ECP, Mihailetchi VD, Blom PWM. Device model for the operation of polymer/fullerene bulk heterojunction solar cells. *Phys Rev B* 2005;72:085205/1–9.
- [34] Chirvase D, Chiguare Z, Knipper M, Parisi J, Dyakonov V, Hummelen JC. Temperature dependent characteristics of poly(3 hexylthiophene)-fullerene based heterojunction organic solar cells. *J Appl Phys* 2003;93:3376.
- [35] Kalita G, Masahiro M, Koichi W, Umeno M. Nanostructured morphology of P3HT:PCBM bulk heterojunction solar cells. *Sol Energy Mater Sol Cells* 2010;54:447–51.
- [36] Garcia-Belmonte G, Munar A, Barea EM, Bisquert J, Ugarte I, Pacios R. Charge carrier mobility and lifetime of organic bulk heterojunctions analyzed by impedance spectroscopy. *Org Electron* 2008;9:847–51.